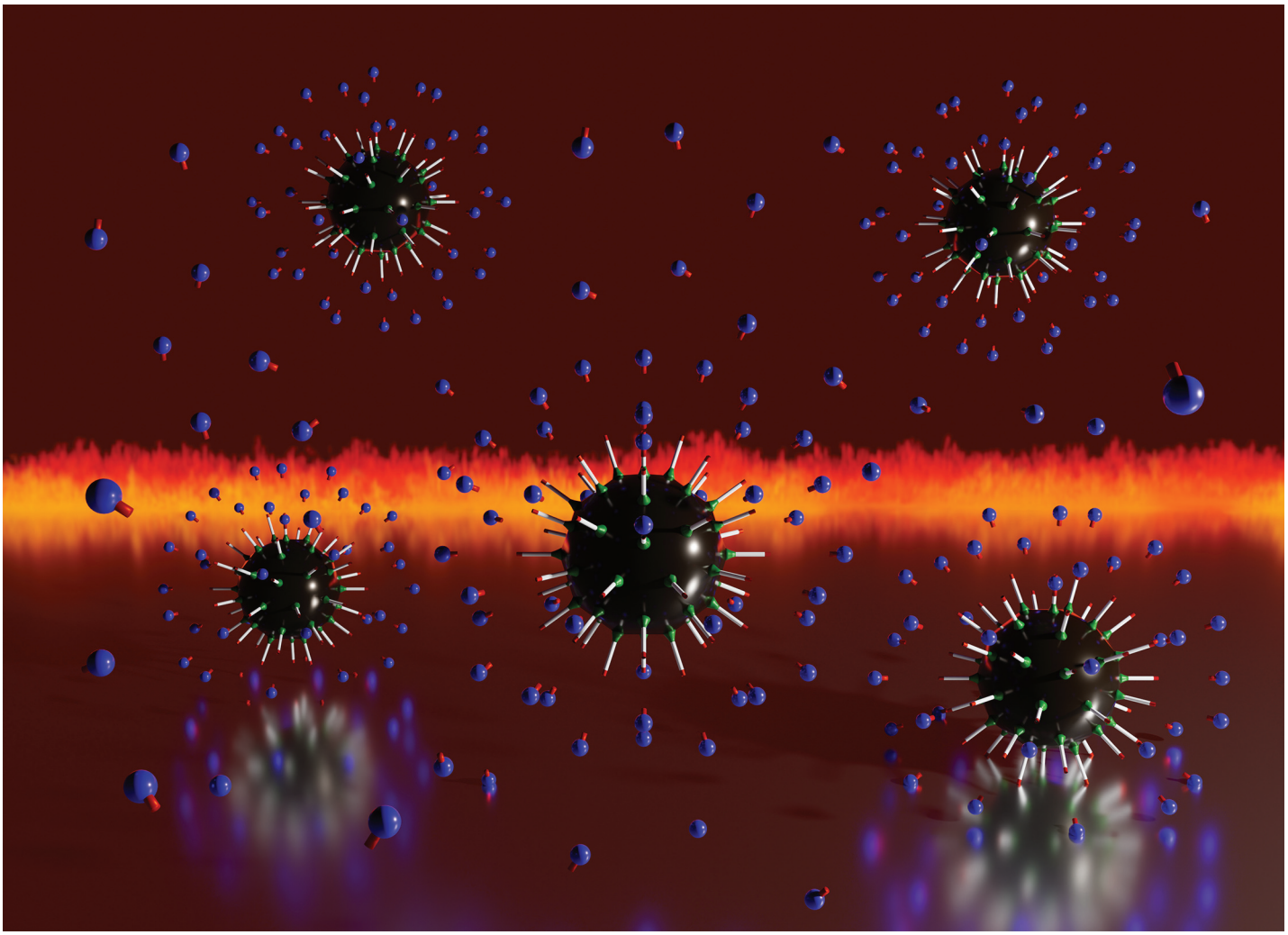

Showcasing research from Prof. Joulia Larionova's and Prof. Sylvain Marque's groups at Institut Charles Gerhardt de Montpellier, Montpellier, France, and at Institut de Chimie Radicalaire, Marseille, France, respectively.

Cascade strategy for triggered radical release by magnetic nanoparticles grafted with thermosensitive alkoxyamine

The design of smart nanoplatforms, consisting of magnetic iron oxide nanoparticles covalently grafted with a thermosensitive radical initiator alkoxyamine, enabled controlled and localized release of free radicals triggered by an alternating current (ac) magnetic field. This was demonstrated by Electronic Paramagnetic Resonance spectroscopy, and investigation of the kinetics of homolysis allowed for comparison between the temperature of alkoxyamine's homolysis and the one measured during the magnetothermia process.

As featured in:

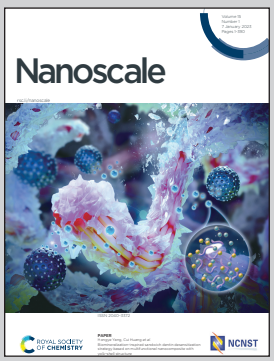

See Gerard Audran, Sylvain R. A. Marque, Joulia Larionova *et al.*, *Nanoscale*, 2023, **15**, 144.

ROYAL SOCIETY OF CHEMISTRY

rsc.li/nanoscale

Registered charity number: 207890

Nanoscale

PAPER

View Article Online
View Journal | View Issue

Check for updates

Cite this: *Nanoscale*, 2023, **15**, 144

Cascade strategy for triggered radical release by magnetic nanoparticles grafted with thermosensitive alkoxyamine†

Basile Bouvet,[a] Saad Sene,[a] Gautier Félix,[a] Jeffrey Havot,[b] Gerard Audran,*[b] Sylvain R. A. Marque,*[b] Joulia Larionova*[a] and Yannick Guari[a]

Received 29th June 2022,
Accepted 20th October 2022

DOI: 10.1039/d2nr03567g

rsc.li/nanoscale

The design of smart nanoplatforms presenting well-definite structures able to achieve controlled cascade action remotely triggered by external stimuli presents a great challenge. We report here a new nanosystem consisting of magnetic iron oxide nanoparticles covalently grafted with a thermosensitive radical initiator alkoxyamine, able to provide controlled and localized release of free radicals triggered by an alternating current (ac) magnetic field. These nanoparticles exhibit a high intrinsic loss power of 4.73 $nHm^2 kg^{-1}$ providing rapid heating of their surface under the action of an ac field, inducing the homolysis of alkoxyamine C–ON bond and then the oxygen-independent formation of radicals. This latter was demonstrated by electronic paramagnetic resonance spectroscopy, and the kinetics of homolysis has been investigated allowing a comparison of the temperature of alkoxyamine's homolysis with the one measured during the magnetothermia process.

Introduction

Nanoparticle-assisted magnetothermia is one of the promising modern nanoscience ways, permitting remote and locally providing important heat activation and control by an external stimulus, an alternating current (ac) magnetic field. This concept is widely exploited in nanomedicine in the hyperthermia treatment of different diseases,[1–4] in environmental applications,[5,6] recently in catalysis,[7–11] in enzymatic reaction,[12–14] and other fields. Among different nanoobjects used as magnetic nanoheaters, iron oxide nanoparticles (IONPs) are the most known in the literature since their composition, size, morphology, and surface state, and therefore, magnetic properties can be precisely controlled. Indeed, they can efficiently convert electromagnetic energy into heat upon exposure even to a biologically acceptable ac field in the 100–300 kHz radiofrequency range with an appropriate field intensity (a few tens of kA m^{-1}).[15] In this connection, the few recent decades have seen extensive development of a new generation of magnetic IONPs with improved magnetic properties specially designed as magnetic nanoheaters with high intrinsic lost power (ILP) values up to 10.42 $nHm^2 kg^{-1}$.[16,17] On the other hand, one-step further traditional magnetothermia has also been performed by designing multifunctional nanoplatforms not only able to combine nanoparticle-assisted heating with another property but also capable of responsively triggering specific cascade processes activated by applying an ac magnetic field. These rather complex systems usually involve the presence of thermosensitive species (such as polymers, liposomes, molecules, and enzymes) grafted or coated on the surface of the magnetic nanoparticles, which benefit from the nanoparticle-assisted temperature increase to trigger another action or more of them in a cascade fashion. Such a strategy is superior to the conventional single-functional approach in terms of controllability, specificity, and efficiency of action and can even benefit from the synergic effects between magnetic heating and triggered action. Such smart systems have mainly and extensively been developed not only for controlled delivery of drugs, nucleic acids, siRNA, or genes usually included in thermoresponsive shells/matrixes,[18–20,21] but also for other applications, such as enzymatic thermal regulation,[22] magnetic separation,[23] environmental applications,[24] chemical/biological catalysis,[25] temperature sensing.[26] In these systems, the magnetic nanoparticle-assisted heating triggers different mechanisms including bond cleavage, matrix transition,

[a]*ICGM, Univ. Montpellier, CNRS, ENSCM, CNRS Montpellier, France. E-mail: joulia.larionova@umontpellier.fr*
[b]*Aix Marseille Univ., CNRS, ICR, UMR 7273, Avenue Escadrille Normandie-Niemen, 13397 Marseille CEDEX 20, France. E-mail: g.audran@univ-amu.fr, sylvain.marque@univ-amu.fr*

†Electronic supplementary information (ESI) available: Estimation of the number of alkoxyamines on the surface of the nanoparticles **3**; quantification of radical's release by EPR analysis; numerical resolution and fit of the homolysis/recombination law; fit of the magnetic nanoparticle-assisted heating and SAR extraction; COSMOL simulation; Fig. S1–S12. See DOI: **https://doi.org/10.1039/d2nr03567g**

Open Access Article. Published on 20 October 2022. Downloaded on 8/2/2025 6:21:49 PM.
This article is licensed under a Creative Commons Attribution-NonCommercial 3.0 Unported Licence.

This journal is © The Royal Society of Chemistry 2023

Open Access Article. Published on 20 October 2022. Downloaded on 8/2/2025 6:21:49 PM.
This article is licensed under a Creative Commons Attribution-NonCommercial 3.0 Unported Licence.

switchable gate, and matrix/shell degradation. However, to the best of our knowledge, the self-generation of radicals remotely triggered by the action of an ac magnetic field, which is interesting for different applications in biomedical and materials fields, has not been reported except for only one example including a large hollow IONP of *ca.* 184 nm loaded with thermosensitive 2,2-azobis[2-(2-imidazolin-2-yl)-propane] molecule, in which, however, the formation of radicals has not been directly demonstrated.[27]

One of the fascinating aspects of magnetothermia is the hypothesis that magnetic nanoparticles behave as "hot spots" in a relatively cold environment.[28] This signifies that the temperature in the close vicinity of the nanoparticle surface submitted under the action of an ac magnetic field can be much higher in comparison to the temperature measured in the solution and the temperature increase is highly localised. Several recent studies have reported the local temperature measurements by employing different means demonstrating the presence of high-temperature gradients from the nanoparticles' surfaces.[26,29–33] Therefore, the authors assumed that it is possible to create hot spots in the very local environment of the nanoparticle surface and trigger the cascade processes in multifunctional magnetic nanosystems at much lower reactor/environmental temperatures. However, the heat diffusion induced by nanoparticles has not yet been clearly established since it depends on numerous factors comprising the ILP value of nanoparticles, solvent nature, and viscosity, a close environment of nanoparticles, the distance between nanoparticles surface and the thermosensitive species and others. For this reason, different systems with well-defined nanoobjects are needed to investigate controlled cascade actions, remotely triggered by an external ac magnetic field.

In this article, we report the design of a new nanosystem, consisting of smart magnetic IONP covalently grafted with a thermosensitive radical initiator alkoxyamine derivative, able to provide localized release of radicals through cascade action, triggered by an ac magnetic field. The external stimulus provided by this latter induces heating of the nanoparticle surface, which sets off the homolysis of the alkoxyamine's C–ON bond affording indeed the oxygen-independent formation of radicals (Fig. 1). We provide a direct demonstration of radicals' release using electronic paramagnetic resonance (EPR) spectroscopy and investigate the kinetics of homolysis allowing to compare the temperature of the alkoxyamine homolysis with the "reactor" temperature during the magnetothermia process.

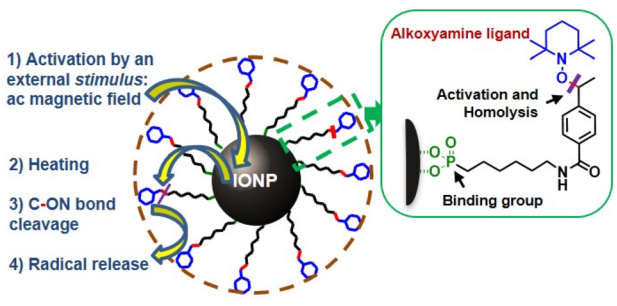

Fig. 1 Schematic representation of IONP@alkoxyamine nanoobjects **3** providing a radical release triggered by an applied ac magnetic field in a cascade action.

Results and discussion

The alkoxyamine derivative carrying the coordinative phosphonic acid function on one hand and the nitroxyl moiety with thermosensitive C–ON bond on the other were chosen here as a pool of radicals because: (i) the thermal lability of the C–ON bond of some alkoxyamines is well documented,[34–37] (ii) they can be covalently anchored to the IONP surface through the coordination of the phosphonate functionality, (iii) when attached to the magnetic nanoparticle's surface, we expect that they will be activated under an ac field at lower reaction temperature since magnetic nanoparticles are able to create hot spots in their local environment, (iv) they may be used as a radical source for biomedical applications since their high potential in the fight against tumors, parasites or bacteria through radicals release triggered by chemical, enzymatic, and physical (light excitation) events[38–43] has recently been demonstrated,[44–46] and the toxicity of non-activated alkoxyamines is low, (v) alkoxyamine may also be used as radical initiators for triggered and controlled polymerization in the systems where the simple heating is not possible.

Note that to the best of our knowledge, the combination of thermosensitive alkoxyamines with magnetic nanoparticles, activated by a magnetic field has never been reported up to date.

The magnetic alkoxyamine grafted nanoparticles, IONP@alkoxyamine, **3** were prepared *via* a two-step approach first involving the synthesis of pristine nanoparticles stabilized by oleic acid (OA) and oleylamine (OL), IONP@OA/OL **1**, through flash thermolysis of the FeO(OH) precursor in *n*-docosane.[47] The post-synthetic covalent grafting of the alkoxyamine derivative **2b** to the surface of the as-obtained IONP was then performed, thanks to its phosphonate group (Fig. 1). The alkoxyamine derivative **2b** was synthesized following a five-step procedure† starting from the commercially available *para*-vinyl benzoic acid, which was esterified with MeOH. Then, the ester was coupled to 2,2,6,6-tetramethylpiperidine 1-oxyl (TEMPO) using Jacobsen's catalyst. The corresponding ester-alkoxyamine was hydrolyzed into the carboxylic derivative, which was transformed into an amide using (6-amino-hexyl)-phosphonic acid diethyl ester **2a**. The phosphonate group was hydrolyzed into (6-{4-[1-(2,2,6,6-tetramethyl-piperidin-1-yloxy)-ethyl]-benzoylamino}-hexyl)-phosphonic acid **2b**.† NMR (^{1}H, ^{13}C, and ^{31}P) and HRMS analyses confirmed the formation of **2a** and **2b**.†

The infrared (IR) spectrum of IONP@alkoxyamine **3** when compared to that of the pristine IONP@OA/OL **1** showed the appearance of new bands in the region between 900 and 1200 cm^{-1},[48–53] which could be ascribed to the P–O vibrations

Open Access Article. Published on 20 October 2022. Downloaded on 8/2/2025 6:21:49 PM.
This article is licensed under a Creative Commons Attribution-NonCommercial 3.0 Unported Licence.

(Fig. S1†). The ν(P–O–Fe) band at 1027 cm^{-1} is consistent with the anchoring of the phosphonate moiety to the surface. Additionally, vibration bands of alkoxyamine **2b**, such as ν(C=O amide) mode at 1633 cm^{-1} [54] or ν(N–O–) mode at 1305 cm^{-1}, were also observed in the IR spectrum of IONP@alkoxyamine **3**, indicating the anchoring of this to the former. The characteristic band at 564 cm^{-1} ascribed to the ν(Fe–O) vibration occurred in the spectra of both, IONP@OA/OL **1** and IONP@alkoxyamine **3**, indicating that the iron oxide remained intact after alkoxyamine grafting. Scanning electron microscopy coupled with EDX (SEM-EDX) analysis validated the successful coating of alkoxyamine on the IONP surface with a Fe/P ratio equal to 98.1/1.9. The estimated number of grafted alkoxyamines per nm^2 is equal to 1.95 (ESI†).

The powder X-ray diffraction (XRD) patterns of the obtained samples **1** and **3** (Fig. S2†) show the reflections, which could be attributed to the Fe_3O_4 phase.[55–57] The calculated lattice constant of 8.38 Å is in agreement with that of the pure magnetite phase. Note that the lattice constants of Fe_3O_4 and γ-Fe_2O_3 are 8.396 (JCPDS 19-629) and 8.351 Å (JCPDS 39-1346), respectively. However, the presence of a thin amorphous layer of maghemite due to surface oxidation cannot be totally excluded.[58] The crystalline domain was calculated from the Scherrer formula, giving an average value of *ca.* 23 nm.

Transmission electronic microscopy (TEM) images of IONP@OA/OL **1** and IONP@alkoxyamine **3** nanoparticles indicate that the size and the pseudo-spherical morphology of IONP have not been altered by the alkoxyamine grafting (Fig. 2a and b). The size distribution histograms provide IONP core sizes, which are equal to 24.91 ± 1.02 and to 25.12 ± 1.07 nm for **1** and **3**, respectively (Fig. S3†). Note that monodispersed nanoparticles were obtained since the standard deviation is lower than 5% for both samples. The dynamic light scattering (DLS) analysis demonstrated the fact that the obtained nanoparticles were well dispersed (Fig. S4†).

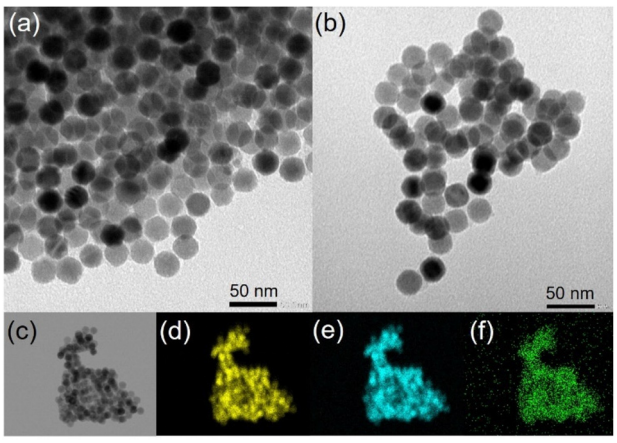

Fig. 2 TEM images of: (a) IONP@OA/OL nanoparticles **1**, (b) IONP@alkoxyamines nanoparticles **3**. (c) HAADF-STEM and (d)–(f) EDX elemental mapping images of IONPs@alkoxyamines nanoparticles **3** with topochemical distribution of Fe (yellow), O (cyan) and P (green).

The topochemical distribution visualized by high-angle annular dark-field scanning transmission electron microscopy (HAADF-STEM) with the energy dispersive X-ray (EDX) mapping confirmed the homogeneous distribution of P atoms from alkoxyamine on the surface of IONP@alkoxyamine **3** nanoparticles (Fig. 2c–f).

The magnetic behavior of nanoparticles **1** and **3** was investigated using powders by using a SQUID-MPMS magnetometer working in the 1.8–350 K temperature range up to 5 T. A classical profile of the temperature dependence of the magnetization performed in the zero-field cooled (ZFC)/field cooled (FC) modes can be observed in Fig. 3a for **3**, indicating that the blocking temperature is situated above 320 K. Note that the ZFC curve does not provide clear evidence of the Verwey transition, which is considered an indication of high purity, good crystallinity, better stoichiometry and the absence of a surface disorder in Fe_3O_4 phase.[58] This may be due to the presence of several phases, low crystallinity, or surface spin disorder. The field dependence of the magnetization at 10 K (red squares) and 300 K (blue squares) (Fig. 3b) show an open hysteresis loop at low temperature (10 K) with a coercive field of 205 Oe, while the hysteresis loop is rather closed at 300 K. The values of the saturation magnetization are equal to 69 and 62 emu g^{-1} (at 5 T) and the coercive field is 428 and 45 Oe at 10 and 300 K, respectively.

Similar features were observed for the non-grafted IONP@OA/OA nanoparticles **1** (Fig. S5†).

The dynamic behavior of **3** was investigated by susceptibility measurements using alternating current (ac) mode in the diluted polyvinylpyrrolidone (PVP) samples (1%) in order to minimize dipolar interparticle interactions. The temperature dependence of the in-phase, χ', and the out-of-phase, χ'', components of the ac susceptibility performed with different frequencies showed two series of peaks, which shift toward higher temperatures as the frequency increases (Fig. S6a and b†). The relaxation time, τ, *vs.* $1/T$ curve clearly showed the occurrence of low and high-temperature magnetic regimes, which indicates the complex dynamic behavior (Fig. S6c†). The low-temperature domain was fitted according to the Néel relaxation model (Fig. S6c†), which relates the blocking temperature to the relaxation time, $\tau = \tau_0 \exp(U/k_BT)$, where $U = KV$ is the energy barrier and τ_0 is the attempt time.[59] The best-fit

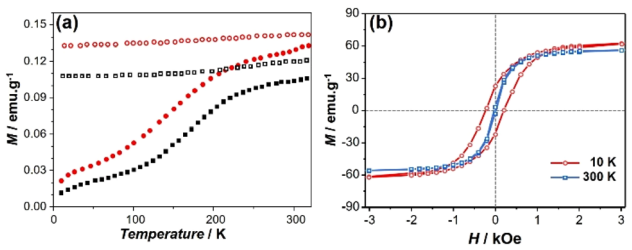

Fig. 3 (a) FC (open symbols)–ZFC curve (full symbols) of IONP@OA/OL (red circles) and IONP@alkoxyamine **3** (black squares) measured under an applied dc magnetic field of 100 Oe, (b) hysteresis loop performed for IONP@alkoxyamine nanoparticles **3** at 10 K (red circles) and 300 K (blue squares) shown between −3 and 3 kOe.

This journal is © The Royal Society of Chemistry 2023

Open Access Article. Published on 20 October 2022. Downloaded on 8/2/2025 6:21:49 PM.
This article is licensed under a Creative Commons Attribution-NonCommercial 3.0 Unported Licence.

parameters gave the value of $U = 10\,443$ cm^{-1} and $\tau_0 = 10^{-24}$ s. The latter value is out of range for the values usually observed for classical superparamagnets (10^{-12} s) and, thus, has no physical meaning. The fit using the Vogel–Fulcher model, $\tau = \tau_0 \exp(U/k_B(T - T_0))$, which takes into account the presence of inter-particles interactions by the introduction of an additional parameter, T_0, gave $U = 4083$ cm^{-1}, $\tau_0 = 10^{-16}$ s and $T_0 = 112$ K. While the τ_0 value is again too small to be acceptable, the decrease in U and τ_0 indicates that dipolar interactions are still present even in the diluted sample. The high-temperature regime cannot be fitted with both models. Such complex dynamic behaviour is probably due to the presence of several phases in the nanoparticles with a spin frustration at the surface and interfaces.

The heating capacity of IONP@alkoxyamine **3** was evaluated by measurements with a thermal camera, the temperature of a suspension of nanoparticles in *tert*-butylbenzene (concentration 4 mg mL^{-1}) under an applied ac magnetic field (≈20 mT at the frequency of 350 kHz) (Fig. S7†). A rapid temperature elevation to 100 °C was observed after 10 minutes of exposure (Fig. 4, red circles). The temperature remained constant (at 100 °C) during the heating reaction (4 h). Note that the *tert*-butylbenzene solvent (reference) did not provide an important temperature increase (Fig. 4, empty black squares). The specific absorption rate (SAR), which represents the heat power produced by the magnetic nanoparticles submitted to an external ac magnetic field, normalized by the mass of these nanoparticles, was estimated using a phenomenological model based on the Newton temperature law with a complex thermal exchange function.† [60,61] The best fit of the *T vs.* time curve has been obtained using the energy exchange function developed with the second order Taylor series (Fig. 4 and Fig. S8, S9†) allowing to extract the SAR value of 420 ± 1 W g^{-1}. The corresponding intrinsic loss power value (ILP) was equal to 4.73 nHm^2 kg^{-1}. This value is situated among the highest ILP values previously published for various magnetic nano-objects.[1]

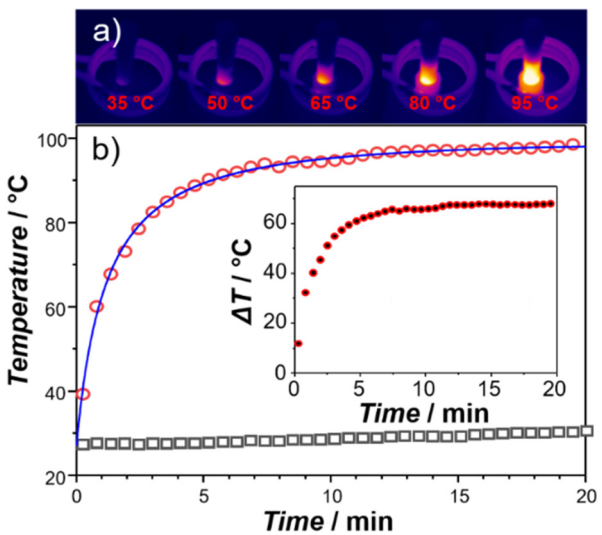

Fig. 4 (a) Thermal images of a vial containing a solution of IONP@alkoxyamine nanoparticles **3** in the presence of the ac magnetic field (350 kHz, 20 mT); (b) temperature measurements as a function of time for an IONP@alkoxyamine suspension **3** (red circles) and *tert*-butylbenzene (black squares) under an ac magnetic field. The blue line represents the best fit with the second-order Taylor series model. Inset: ΔT *vs.* time curve, where ΔT represents the difference between the temperature between the reference solution and the solution of nanoparticles **3**.

A cascade action consisting of a radical production under magnetic nanoparticle-assisted heating was demonstrated using the EPR technique. First, investigations on the free alkoxyamine were performed in order to provide evidence for the formation of radicals upon thermal heating and to determine its kinetics. The *tert*-butylbenzene solution of the ethylated derivative of alkoxyamine **2a** was used for these experiments for the sake of consistency with further investigations of alkoxyamine-grafted nanoparticles **3** since **2b** is weakly soluble in this solvent. For this, the *tert*-butylbenzene solution (10^{-4} M) of alkoxyamine was heated at 115 °C for 5.5 h and the homolysis reaction was monitored by EPR spectroscopy. The EPR spectra recorded during the heating showed a classical three-line profile coming from the hyperfine coupling of the odd electron with the nitrogen atom of nitroxide (Fig. S10a–c,† red line) and corresponding to what is expected for nitroxide radicals ($I_N = 1$, $S = \frac{1}{2}$) generated by the cleavage of the thermosensitive C–ON bond.[62] The hyperfine coupling constant is equal to $a_N = 16.7$ G, which is fully consistent with nitroxide. In comparison, the EPR spectrum of **2a** before heating is silent, indicating that no radicals can be formed without an applied stimulus, confirming the good stability of the alkoxyamine. Given that the intensity of an EPR signal is directly proportional to the number of radicals formed in solution, this technique allows monitoring the evolution of radicals' concentration. The curve of the normalized nitroxide concentration (C/C_0) *vs.* time (Fig. S10c†) indicates that alkoxyamine **2a** exhibits mono-exponential kinetics (eqn (1)):

$$[\text{nitroxide}]_t = [\text{nitroxide}]_\infty(1 - e^{-k_d t}) \quad (1)$$

where k_d is the rate homolysis constant, t is the time, [nitroxide] is the concentration of the generated nitroxide during homolysis. The fitting of the experimental curve with eqn (1) affords $k_d = 7.0 \times 10^{-4}$ s^{-1} at 115 °C (91% conversion). Then, the Arrhenius eqn (2):

$$E_a = -RT \ln\left(\frac{k_d}{A}\right) \quad (2)$$

(where E_a is the activation energy, $A = 2.4 \times 10^{14}$ s^{-1} is the pre-exponential factor in the case of the alkoxyamine homolysis) allows to estimate $E_a = 130.3$ kJ mol^{-1} and, subsequently, the half-life time $t_{1/2} = 15.6$ years at 20 °C.

Second, the *tert*-butylbenzene solution of IONP@alkoxyamine nanoparticles **3** (4 mg mL^{-1}) was subjected to the action of an ac magnetic field (20 mT, 350 kHz), and the formation of the radicals with time was monitored by EPR by sampling at various time intervals.† Note that the aliquots were cooled and the magnetic nanoparticles were

Open Access Article. Published on 20 October 2022. Downloaded on 8/2/2025 6:21:49 PM.
This article is licensed under a Creative Commons Attribution-NonCommercial 3.0 Unported Licence.

removed from solutions using a magnet, thus leaving the formed nitroxyl radicals in the solutions (see Fig. 5a). Their EPR spectra exhibited three lines with increasing time intensities expected for the release of the nitroxides (Fig. 5b, red line), while in the spectrum collected before the action of the ac magnetic field the lines were absent (Fig. 5b, black line). An identical result was obtained when the solution of IONP@alkoxyamine nanoparticles **3** was heated up to 110 °C for 2 h (Fig. S11†). This result indicates that IONP@alkoxyamine nanoparticles **3** are perfectly stable without the application of external stimuli and start to provide radicals only when triggered by the action of the magnetic field or thermal heating. The C/C_0 *vs.* time curve (Fig. 5c) obtained for IONP@alkoxyamine **3** triggered by the magnetic field shows an S-shape in the early stage of the experiment and a bell-shape after around 70% conversion. The bell-shaped curve shape of nitroxyl radical concentration may be explained by a combination of two phenomena. The first is the production of nitroxyl radicals by homolysis from alkoxyamine reactants (k_d chemical constant), and the second is the nitroxyl radical degradation (noted k_1). When all alkoxyamine reactants are consumed the nitroxyl radical production is stopped, leading to a decrease of the nitroxyl radical concentration curve. Assuming that the side-reaction is of pseudo-first order, the evolution of the concentrations in alkoxyamine and nitroxyl radicals with time is given by eqn (3) and (4), respectively:

$$\frac{d[\text{alkox}]}{dt} = -k_d[\text{alkox}] \quad (3)$$

$$\frac{d[\text{nitroxide}]}{dt} = k_d[\text{alkox}] - k_1[\text{nitroxide}] \quad (4)$$

On the other hand, the S-shaped curve in the early stages points at a certain delay in the radicals' production, which might be ascribed to the fact that at the beginning, the final and stable temperature of homolysis at the surface of nanoparticles is not yet achieved. The experimental curve was fitted by eqn (3) and (4) taking into account that the homolysis rate constant, k_d, follows the Arrhenius law with a temperature dependence on time (eqn (5)):

$$k_d = A \times \exp(-E_a/RT(t)) \quad (5)$$

where $T(t)$ represents the variation of the temperature on the surface of the nanoparticles as a function of time. We took the approximation that the temperature at the nanoparticle surface obeys the Newton temperature law:

$$T(t) = (T_{max} - T_0)(1 - \exp(-t/\tau_T)) + T_0 \quad (6)$$

where T_0 is the initial temperature (20 °C), T_{max} is the maximal temperature and τ_T is the heating rate. Note that the previously obtained values of A and E_a in the free alkoxyamine experiments were used here to estimate the temperature at the surface of the nanoparticles. Eqn (5) and (6) were solved numerically because of the inexistence of an analytical solution. The following parameters, T_{max} = 110 ± 1 °C, k_1 = (8.12 ± 0.35) × 10^{-5} s^{-1}, k_d = 4.14 × 10^{-4} were obtained. The extracted k_d value observed under the action of the ac magnetic field corresponds to an expected temperature of 110 °C after 3 hours of experiments for complete homolysis of **3** (Fig. 5), whereas the temperature of 100 °C was measured by the thermal camera in the solution (the expected for 100 °C k_d is equal to 1.38 × 10^{-4} s^{-1}) (Fig. S12†). This indicates that the temperature in a few nm thick corona around the nanoparticles seems to be higher than the one measured for the bulk of the solution. While the literature reports rather controversial conclusions on the heating diffusion from magnetic nanoparticle surfaces. Note that, in our system and for the measured conditions, the temperature difference is not as pronounced as reported in the previously published works.[28,32,63] This difference may probably be explained by the relatively long time of heating, the different nature of the solvent, the rather long distance between the nanoparticle surface and C–ON bond, and the modulation of these factors can be further explored. Therefore, our IONP-grafted alkoxyamine system may be considered as the first step toward a systematic investigation of heat diffusion during magnetothermia.

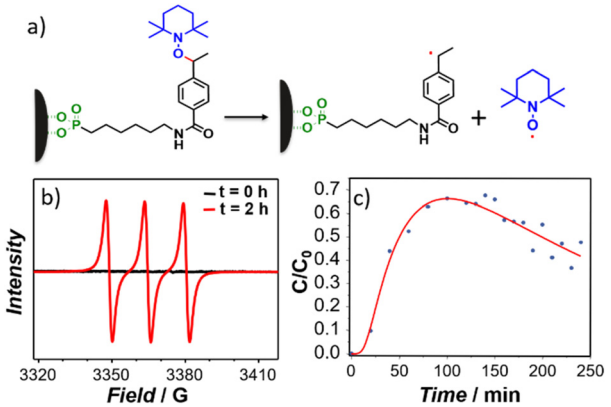

Fig. 5 (a) Schematic representation of radical formation for IONP@alkoxyamine **3** under external stimuli; (b) EPR spectra for the *tert*-butylbenzene solution of IONP@alkoxyamine nanoparticles **3** (4 mg mL^{-1}) before (black) and after the action of an ac magnetic field (20 mT, 350 kHz) (red); (c) the curve C/C_0 *vs.* time for IONP@alkoxyamine nanoparticles **3** under the ac magnetic field.

Conclusion

In summary, we report a model nanosystem able to provide a localized radical release remotely triggered by an external stimulus through a cascade action. It consists of magnetic iron oxide nanoparticles covalently grafted with a thermosensitive alkoxyamine derivative, which under a controlled action of an ac magnetic field, provides important heating of the nanoparticle surface conducting on the homolysis of the thermosensitive C–ON bond of alkoxyamine and then the formation of radicals in an oxygen-independent way. It should be noted that the obtained nanoparticles of *ca.* 25 nm are monodispersed and present a well-definite quasi-spherical shape. The macroscopic heating of up to 100 °C for the nanoparticles' col-

This journal is © The Royal Society of Chemistry 2023

Open Access Article. Published on 20 October 2022. Downloaded on 8/2/2025 6:21:49 PM.
This article is licensed under a Creative Commons Attribution-NonCommercial 3.0 Unported Licence.

loidal solution was realized by applying an ac magnetic field achieving the desired temperature after 10 min of exposure. The obtained ILP value of 4.73 $nHm^2\ kg^{-1}$ permits the placement of these nanoparticles among the most powerful magnetite-based magnetic nanoheaters. The radical formation has been evidenced by EPR spectroscopy on the free alkoxyamine molecule upon heating and on grafting alkoxyamine IONP on the nanoparticles under an applied magnetic field. A difference of 10 °C between the local temperature on the surface of the nanoparticles and the bulk solution was noted. The nanosystem model described here opens important perspectives in (i) the biomedical field and especially for the treatment of cancer or bacteria-related diseases, (ii) the investigation of heating confinement and heating diffusion using thermosensitive alkoxyamines as temperature probes, and (iii) the polymerization reactions for the development of a surface-initiated nitroxide-mediated polymerization.

Experimental

Syntheses

Materials. All chemical reagents were purchased and used without further purification: ferric hydroxide oxide (FeO(OH) hydrated, 30–50 mesh), oleic acid (90%), and oleylamine (90%) from Sigma Aldrich; *n*-docosane (99%) from Acros Organic. Pentane, diethyl ether, cyclohexane, acetone, and ethanol were purchased from Merck.

All organic reagents and solvents were purchased from commercial suppliers (Sigma-Aldrich, Sikémia, and TCI). All organic chemical experiments were performed under anhydrous conditions and an inert atmosphere of argon and, except where stated, using a dried apparatus, and employing standard techniques for handling air-sensitive materials. Chemicals were purchased from Sigma-Aldrich, TCI, or Sikémia and were used as received. Routine reaction monitoring was performed using silica gel 60 F254 TLC plates; the spots were visualized upon exposure to UV light and a *p*-anisaldehyde or phosphomolybdique acid solution in EtOH followed by heating. Purifications were performed on chromatography columns with silica gel grade 60 (230–400 mesh). ^{1}H nuclear magnetic resonance (NMR) spectra were recorded using an internal deuterium lock at ambient temperatures on the following instruments: Bruker AC400 (400 MHz). Data are presented as follows: chemical shift (in ppm), integration, multiplicity (s = singlet, d = doublet, t = triplet, m = multiplet, br = the signal is broad, dd = doublet of doublets), coupling constant (J in Hz) and integration. ^{13}C nuclear magnetic resonance (NMR) spectra were recorded using an internal deuterium lock at ambient temperatures on the following instruments: Bruker AC400 (101 MHz). ^{31}P nuclear magnetic resonance (NMR) spectra were recorded on a Bruker AC400 (162 MHz) spectrometer with complete proton decoupling. High-resolution mass spectra (HRMS) were recorded on an SYNAPT G2 HDMS (Waters) spectrometer equipped pneumatically-assisted atmospheric pressure ionization source (API). Samples were ionized using the positive electrospray mode as follows: electrospray tension (ISV): 2800 V; opening tension (OR): 20 V; nebulization gas pressure (nitrogen): 800 L h^{-1}. Low-resolution mass spectra were recorded on an ion trap AB SCIEX 3200 QTRAP equipped with an electrospray source. The parent ion (M^+, $[M + H]^+$, $[M + Na]^+$ or $[M + NH_4]^+$) is quoted.

Syntheses of the alkoxyamines 2a, 2b, and alkoxyamine-grafted nanoparticles 3. Methyl 4-vinylbenzoate. A solution of 4-vinylbenzoic acid (3.00 g, 20.3 mmol, 1 eq.) and K_2CO_3 (27.4 g, 198.5 mmol, 9.8 eq.) were stirred under Ar, at r.t. Then, iodomethane (1.50 mL, 24.3 mmol, 1.2 eq.) was added slowly. The reaction was controlled by TLC (5% MeOH in DCM). After the reaction, water was added to the reaction mixture, and the reaction mixture was extracted with Et_2O. The organic layer was washed with water and dried on $MgSO_4$, and the solvent was removed under a vacuum. The crude was purified by column chromatography (DCM/MeOH gradient from 0% to 5% of MeOH) to yield methyl-4-vinylbenzoate quantitatively. The ^{1}H spectra of this compound were identical to the one reported.[1] ^{1}H NMR (300 MHz, $CDCl_3$): δ 8.10–7.89 (m, 2H, aromatics), 7.52–7.39 (m, 2H, aromatics), 6.86–6.62 (dd, J = 17.6, 10.9 Hz, 1H, CH═CH_2), 5.86 (dd, J = 17.6, 0.7 Hz, 1H, CH═CH_2), 5.38 (dd, J = 10.9, 0.7 Hz, 1H, CH═CH_2), 3.91 (s, 3H, $COOCH_3$).

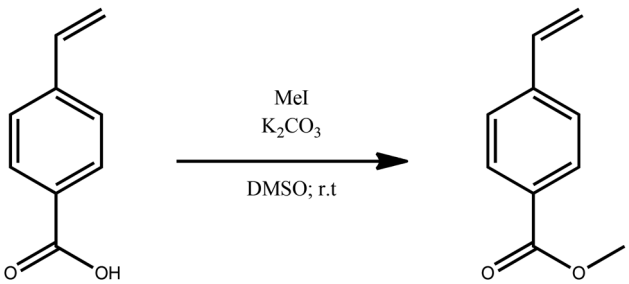

Methyl 4-(1-((2,2,6,6-tetramethylpiperidin-1-yl)oxy)ethyl)benzoate. In an open-air flask, $MnCl_2$ (163 mg, 0.82 mmol, 0.1 eq.) was added to a stirred solution of salen ligand (221 mg, 0.82 mmol, 0.1 eq.) in iPrOH. After 30 minutes of stirring at room temperature, a solution of 2,2,6,6-tetramethylpiperidine 1-oxyl radical (TEMPO) (1.28 g, 8.2 mmol, 1 eq.) and methyl 4-vinylbenzoate (2.0 g, 12.3 mmol, 1.5 eq.) in iPrOH was added, then, $NaBH_4$ powder (4 eq.) was added in small portions. The resulting suspension was stirred at room temperature for 6 h. It was then diluted with EtOAc and 1 M aq. HCl was carefully added. Solid $NaHCO_3$ was then added until neutralization. The layers were separated, and the organic phase was washed with water and brine and dried over Na_2SO_4. After concentrating under reduced pressure, the residue was purified by column chromatography (EP/Et_2O gradient from 0% to 6% of Et_2O) to yield methyl 4-(1-((2,2,6,6-tetramethylpiperidin-1-yl)oxy)ethyl)benzoate (1.35 g, 34%). ^{1}H NMR (300 MHz, $CDCl_3$): δ 8.01–7.96 (m, 2H, aromatics), 7.40–7.35 (m, 2H, aromatics), 4.82 (q, J = 6.7 Hz, 1H, CH–CH_3), 3.90 (s, 3H, $COOCH_3$), 1.30–1.60 (m, 6H, 3 × CH_2), 1.47 (d, J = 6.7, 3H, CH–CH_3), 1.29 (br s, 3H, C–CH_3), 1.17 (br s, 3H, C–CH_3), 1.02 (br s, 3H, C–CH_3), 0.62 (br s, 3H, C–CH_3). ^{13}C NMR (75 MHz,

Open Access Article. Published on 20 October 2022. Downloaded on 8/2/2025 6:21:49 PM.
This article is licensed under a Creative Commons Attribution-NonCommercial 3.0 Unported Licence.

$CDCl_3$): δ 167.3 (CO), 151.3 (C), 129.6 (2 × $CH_{aromatic}$), 128.8 (C), 126.6 (2 × $CH_{aromatic}$), 83.1 (CH), 59.8 (2 × C), 52.1 (CH_3), 40.5 (2 × CH_2), 34.6 (CH_3), 34.3 (CH_3), 23.7 (CH_3), 20.4 (2 × CH_3), 17.3 (CH_2). HRMS (ESI): calc. $[M + H]^+$: 320.2220; found: 320.2218.

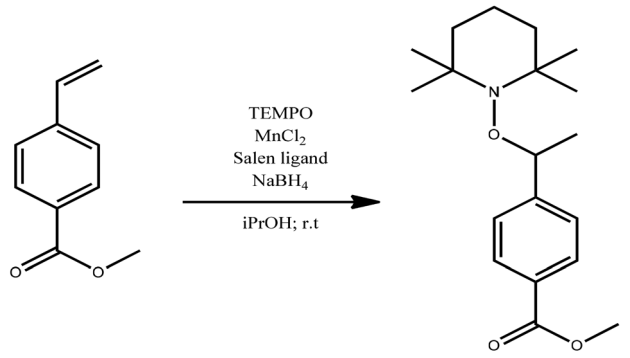

4-(1-((2,2,6,6-Tetramethylpiperidin-1-yl)oxy)ethyl)benzoic acid. KOH (0.84 g, 15 mmol, 8 eq.) was added to a solution of the ester-based alkoxyamine (0.60 g, 1.88 mmol, 1 eq.) in THF–H_2O (1 : 1) at room temperature. The mixture was stirred at 30 °C overnight and then acidified with 1 M HCl. The mixture was diluted with water and extracted with DCM. The combined organic phase was dried on $MgSO_4$ and the solvent was evaporated. The crude was purified by column chromatography (DCM : MeOH gradient from 0% to 5% of MeOH) to yield 4-(1-((2,2,6,6-tetramethylpiperidin-1-yl)oxy)ethyl)benzoic acid quantitatively (570 mg). ^{1}H NMR (300 MHz, $CDCl_3$): δ 8.01–7.96 (m, 2H, aromatics), 7.40–7.35 (m, 2H, aromatics), 4.85 (q, J = 6.7 Hz, 1H, CH–CH_3), 1.43–1.23 (m, 6H, 3 × CH_2) 1.49 (d, J = 6.7 Hz, 3H, CH–CH_3), 1.30 (br s, 3H, C–CH_3), 1.18 (br s, 3H, C–CH_3), 1.03 (br s, 3H, C–CH_3), 0.64 (br s, 3H, C–CH_3). ^{13}C NMR (75 MHz, $CDCl_3$): δ 172.1 (CO), 152.2 (C), 130.3 (2 × $CH_{aromatic}$), 128.0 (C), 126.7 (2 × $CH_{aromatic}$), 83.1 (CH), 59.9 (2 × C), 40.4 (2 × CH_2), 34.5 (CH_3), 34.3 (CH_3), 23.74 (CH_3), 20.50 (2 × CH_3), 17.31 (CH_2). HRMS (ESI): calc. $[M + H]^+$: 306.2064; found: 306.2059.

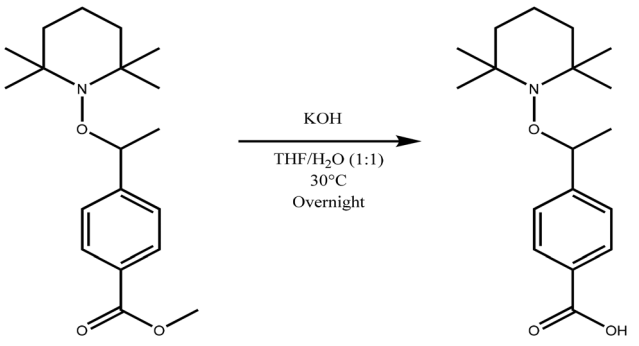

Diethyl(6-(4-(1-((2,2,6,6-tetramethylpiperidin-1-yl)oxy)ethyl) benzamido)hexyl)-phosphonate 2a. DMAP (0.30 g, 2.46 mmol, 1.5 eq.) was added to a stirred solution of alkoxyamine (501 mg, 1.64 mmol, 1 eq.) in DCM (5 mL) and the solution was stirred at room temperature under argon for 10 min. After the addition of EDCI (382 mg, 0.43 mL, 2.46 mmol, 1.5 eq.), the solution was stirred at room temperature for a further 30 min, then, the amine (388 mg, 1.64 mmol, 1.5 eq.) was added at 0 °C. The reaction mixture was stirred at room temperature overnight. The mixture was washed with HCl 1 M, $NaHCO_3$ (saturated solution), distilled water, and brine. The organic phase was dried with $MgSO_4$, and the solvent was removed under a vacuum. The purification by column chromatography (DCM/MeOH from 0% to 6% of MeOH) yielded diethyl(6-(4-(1-((2,2,6,6-tetramethylpiperidin-1-yl)oxy)ethyl)benzamido)hexyl)phosphonate (0.800 g, 99%). ^{1}H NMR (300 MHz, $CDCl_3$): δ 7.73–7.69 (m, 2H, aromatics), 7.33–7.37 (m, 2H, aromatics), 6.62 (t, J = 5.6 Hz, 1H, amide), 4.76 (q, J = 6.7 Hz, 1H, CH–CH_3), 4.18–3.87 (m, 4H, 2 = O–CH_2–CH_3), 3.38 (dd, J = 13.1, 6.9 Hz, 2H), 1.75–1.05 (m, 16H), 1.41 (d, J = 6.7 Hz, 3H, CH–CH_3), 1.26 (t, J = 7.1 Hz, 6H, 2 × O–CH_2–CH_3), 1.19 (br s, 3H, C–CH_3), 1.1 (br s, 3H, C–CH_3), 0.97 (br s, 3H, C–CH_3), 0.59 (br s, 3H, C–CH_3). ^{13}C NMR (75 MHz, $CDCl_3$): δ 167.62 (CO), 149.54 (C), 133.31 (C), 126.88 (2 × $CH_{aromatic}$), 126.70 (2 × $CH_{aromatic}$), 83.02 (CH), 61.59 (CH_2), 61.52 (CH_2), 59.82 (2 × C), 40.44 (2 × CH_2), 39.90 (CH_2), 34.55 (CH_3), 34.40 (CH_3), 30.13 (d, J_{C-P} = 16.18 Hz, CH_2), 29.52 (CH_2), 26.44 (CH_2), 25.59 (d, J_{C-P} = 140.60 Hz, CH_2), 23.75 (CH_3), 22.41 (d, J_{C-P} = 5.15 Hz, CH_2), 20.43 (2 × CH_3), 17.28 (CH_2), 16.62 (CH_3), 16.58 (CH_3). ^{31}P NMR (162 MHz, $CDCl_3$): δ 32.33. HRMS (ESI): calc. $[M + H]^+$: 525.3452; found: 525.3455.

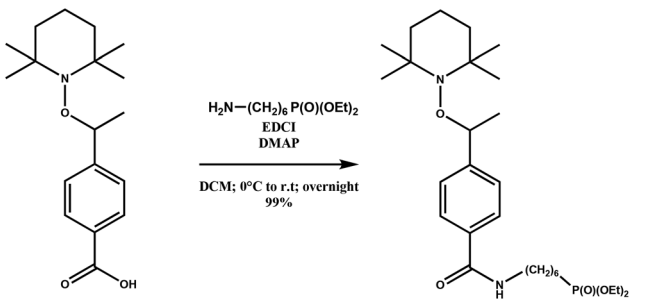

(6-(4-(1-((2,2,6,6-Tetramethylpiperidin-1-yl)oxy)ethyl)benzamido) hexyl)phosphonic acid 2b. The phosphonate-based alkoxyamine (0.80 g, 1.52 mmol, 1 equiv.) was dissolved in dichloromethane (15 mL) and cooled at −20 °C. Then, TMSBr (300 µL, 3.3 equiv.) was added and the reaction was stirred overnight at room temperature. The solvent was evaporated under reduced pressure and the residual mixture was dissolved in methanol (20 mL) and stirred for 30 min. The solvent was evaporated under reduced pressure to yield alkoxyamine **2b** as a clear oil, which was pure enough to be used without further purification in the next step (680 mg, 96%). ^{1}H NMR (300 MHz, MeOD): δ 7.91–7.85 (m, 2H, aromatics), 7.62–7.56 (m, 2H, aromatics), 5.88 (q, J = 6.4 Hz, 1H, CH–CH_3), 1.20–2.30 (m, 18H), 1.77 (s, 3H, C–CH_3), 1.72 (d, J = 6.4 Hz, 3H, CH–CH_3), 1.50 (s, 3H, C–CH_3), 1.29 (s, 3H, C–CH_3), 1.06 (s, 3H, C–CH_3). ^{13}C NMR (75 MHz, MeOD): δ 169.18 (CO), 145.18 (C), 135.95 (C), 128.86 (2 × CH), 127.90 (2 × CH), 87.22 (CH), 72.90 (C), 72.27 (C), 40.88 (CH_2), 38.08 (CH_2), 37.99 (CH_2), 31.2 (d, J_{C-P} = 16.57 Hz, CH_2), 30.17 (CH_2), 29.41 (CH_3), 29.18 (CH_3), 27.81 (d, J_{C-P} = 137.03 Hz, CH_2), 27.52 (CH_2), 23.99 (CH_3), 23.70 (d, J_{C-P} = 4.91 Hz, CH_2), 21.09 (CH_3), 20.92 (CH_3), 16.41 (CH_2). ^{31}P NMR

This journal is © The Royal Society of Chemistry 2023

Open Access Article. Published on 20 October 2022. Downloaded on 8/2/2025 6:21:49 PM.
This article is licensed under a Creative Commons Attribution-NonCommercial 3.0 Unported Licence.

(121 MHz, MeOD): δ 30.19. HRMS (ESI) calc. $[M + H]^+$: 469.2826; found: 469.2824.

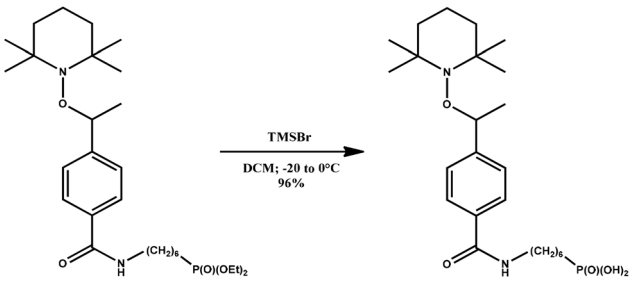

Synthesis of pristine iron oxide nanoparticles IONP@OA/OL 1. The synthesis of Fe_3O_4 nanoparticles surrounded by OA and OL was performed following a modified thermal decomposition method reported previously.[2] First, 0.18 g of FeO(OH) (2 mmol), 3.17 g of oleic acid (10 mmol), and 5.02 g of *n*-docosane were mixed and degassed under vacuum for 30 min with magnetic stirring. Subsequently, the mixture was then heated to 350 °C under argon flow at a heating rate of 10 °C min^{-1} and maintained at 350 °C for 90 min under stirring and argon flow. The heating was turned off and the mixture was then allowed to cool under air. When the temperature reached 200 °C, the heating was turned on again and the temperature was maintained at 180 °C for a further 90 min to realise complete oxidation of the nanoparticles (from FeO to Fe_3O_4). The heating was then turned off and the mixture was allowed to cool under air. When the temperature was around 50 °C, 15 mL of pentane was added and the nanoparticles were separated by magnetic decantation. The nanoparticles were then washed three times by dispersion in diethyl ether, followed by magnetic decantation. The resultant IONP@OA/OL was finally dispersed in 15 mL of cyclohexane and 200 μL of oleylamine was added for colloidal stabilization.

Synthesis of IONP@alkoxyamine 3. The grafting of the alkoxyamine derivative **2b** on the surface of **1** was performed by a ligand exchange method. For this, **2b** (200 mg) was dissolved in 20 mL of THF/MeOH (95/5 (vol%)), and mixed with **1** suspended in THF (1 mg ml^{-1} in 20 mL). The mixture was then sonicated for 10 min and rotary stirred at 300 rpm at room temperature for 48 hours. The grafted nanoparticles were then collected by magnetic separation and washed three times with MeOH. The nanoparticles were then stored in MeOH or dried for further characterization.

Characterization

The size and shape of the nanoparticles were observed using transmission electron microscopy (TEM) at 100 kV (LaB_6 JEOL 1400 Flash). Dynamic light scattering (DLS) measurements were performed on a Zetasizer Nano-series from Malvern instruments (ZEN3600) in order to determine the hydrodynamic diameter of the nanoparticles. Powder X-ray diffraction (PXRD) studies were performed using a PANalytical X'Pert Powder analytical diffractometer mounted in a Debye–Scherrer configuration and equipped with Cu radiation (λ = 1.5418 Å). Infrared spectra using attenuated total reflectance (ATR-IR) were recorded using a PerkinElmer FT-IR spectrometer. Quantifications of P and Fe elements were performed using a Scanning electron microscope equipped with an Energy Dispersive X-Ray analyser (SEM-EDX) on an FEI Quanta FEG 200 instrument. The powders were deposited on an adhesive carbon film and analysed under a vacuum. RMN analyses were performed with a Bruker AC400 (400 MHz) instrument. Magnetic measurements were performed using a SQUID MPMS-XL magnetometer working in the temperature range 1.8–350 K up to 5 T by using static (direct current (dc)) and dynamic (alternating current (ac)) modes. The data were corrected by the sample holder. The ac magnetic susceptibility measurements were carried out under a 3.5 Oe oscillating field without the external dc field for samples diluted in polyvinylpyrrolidone (PVP) (1 wt%). Temperatures associated with relaxation times ($1/(2\pi f)$) were extracted from the out-of-phase ac magnetic susceptibility, and the fit of the relaxation times was realized using the Néel law:

$$\tau = \tau_0 \exp\left(\frac{U}{k_B T}\right) \rightarrow \ln(\tau) = \ln(\tau_0) + \frac{U}{k_B T}$$

or the Vogel–Fulcher law:

$$\tau = \tau_0 \exp\left(\frac{U}{k_B (T - T_0)}\right) \rightarrow \ln(\tau) = \ln(\tau_0) + \frac{U}{k_B (T - T_0)}$$

where U is the barrier energy in cm^{-1}.

Hyperthermia properties were studied using an electromagnetic field of 20 mT at 340 kHz. A thermal camera OPTRIS PI 450i was used to record temperature elevation during hyperthermia measurements. Electronic paramagnetic resonance (EPR) was performed using the Elexsys E500 CW spectrometer from Bruker, in the X band (around 9.8 GHz), dressed with a resonant cavity ER4122SHQ. Samples were analysed using 50 μL capillary tubes (from Hirschmann), sealed with silicon paste. Samples were carefully placed in the same positions. Analyses were made at room temperature, with a window of 10 mT (100 G) centered around g = 2, an amplitude of 1 G, a frequency of 100 kHz, and a microwave power of 10 db.

Author contributions

Conceptualization, G. A., S. M., J. L. and Y. G.; methodology, G. A., S. M., J. L. and G. F.; software, G. F.; validation, S. S., B. B. and J. H.; investigation, S. S., B. B. and J. H. resources, G. A., S. M., J. L, Y. G.; data curation, B. B. and J. H.; writing—original draft preparation, J. L.; writing—review and editing, G. A., S. M., J. L. and Y. G.; visualization, S. S., G. F., B. B. and J. H.; supervision, S. S., G. F., G. A., S. M., J. L. and Y. G.; project administration, G. A., S. M., J. L. and Y. G.; funding acquisition, G. A., S. M., J. L. and Y. G.

Conflicts of interest

There are no conflicts to declare.

Open Access Article. Published on 20 October 2022. Downloaded on 8/2/2025 6:21:49 PM.
This article is licensed under a Creative Commons Attribution-NonCommercial 3.0 Unported Licence.

Acknowledgements

The authors thank the University of Montpellier, the University of Aix Marseille, the CNRS and the Agence Nationale de la Recherche (ANR-17-CE18-0017 and ANR-22-CE09-0026) financial support. The authors are grateful to the Platform of Analysis and Characterization (PAC) of ICGM for magnetic and X-ray diffraction measurements.

Notes and references

1 H. Gavilán, S. K. Avugadda, T. Fernández-Cabada, N. Soni, M. Cassani, B. T. Mai, R. Chantrell and T. Pellegrino, *Chem. Soc. Rev.*, 2021, **50**, 11614–11667.
2 T. Ibelli, S. Templeton and N. Levi-Polyachenko, *Int. J. Hyperthermia*, 2018, **34**, 144–156.
3 E. A. Périgo, G. Hemery, O. Sandre, D. Ortega, E. Garaio, F. Plazaola and F. J. Teran, *Appl. Phys. Rev.*, 2015, **2**, 041302.
4 C. Xu, O. U. Akakuru, J. Zheng and A. Wu, *Front. Bioeng. Biotechnol.*, 2019, **7**, 141.
5 A. Gallo-Cordova, J. J. Castro, E. L. Winkler, E. Lima, R. D. Zysler, M. d. P. Morales, J. G. Ovejero and D. A. Streitwieser, *J. Cleaner Prod.*, 2021, **308**, 127385.
6 M. Munoz, J. Nieto-Sandoval, E. Serrano, Z. M. de Pedro and J. A. Casas, *J. Environ. Chem. Eng.*, 2020, **8**, 104085.
7 L. M. Martínez-Prieto, J. Marbaix, J. M. Asensio, C. Cerezo-Navarrete, P.-F. Fazzini, K. Soulantica, B. Chaudret and A. Corma, *ACS Appl. Nano Mater.*, 2020, **3**, 7076–7087.
8 J. Marbaix, N. Mille, L.-M. Lacroix, J. M. Asensio, P.-F. Fazzini, K. Soulantica, J. Carrey and B. Chaudret, *ACS Appl. Nano Mater.*, 2020, **3**, 3767–3778.
9 J. Lee, S. Dubbu, N. Kumari, A. Kumar, J. Lim, S. Kim and I. S. Lee, *Nano Lett.*, 2020, **20**, 6981–6988.
10 A. Meffre, B. Mehdaoui, V. Connord, J. Carrey, P. F. Fazzini, S. Lachaize, M. Respaud and B. Chaudret, *Nano Lett.*, 2015, **15**, 3241–3248.
11 S. Ceylan, C. Friese, C. Lammel, K. Mazac and A. Kirschning, *Angew. Chem., Int. Ed.*, 2008, **47**, 8950–8953.
12 I. Armenia, M. V. Grazú Bonavia, L. De Matteis, P. Ivanchenko, G. Martra, R. Gornati, J. M. de la Fuente and G. Bernardini, *J. Colloid Interface Sci.*, 2019, **537**, 615–628.
13 M. Suzuki, H. Hayashi, T. Mizuki, T. Maekawa and H. Morimoto, *Biochem. Biophys. Rep.*, 2016, **8**, 360–364.
14 M. Suzuki, A. Aki, T. Mizuki, T. Maekawa, R. Usami and H. Morimoto, *PLoS One*, 2015, **10**, e0127673.
15 S. V. Spirou, M. Basini, A. Lascialfari, C. Sangregorio and C. Innocenti, *Nanomaterials*, 2018, **8**, 401.
16 P. Guardia, A. Riedinger, S. Nitti, G. Pugliese, S. Marras, A. Genovese, M. E. Materia, C. Lefevre, L. Manna and T. Pellegrino, *J. Mater. Chem. B*, 2014, **2**, 4426–4434.
17 G. Salas, J. Camarero, D. Cabrera, H. Takacs, M. Varela, R. Ludwig, H. Dähring, I. Hilger, R. Miranda, M. d. P. Morales and F. J. Teran, *J. Phys. Chem. C*, 2014, **118**, 19985–19994.
18 M. Moros, J. Idiago-López, L. Asín, E. Moreno-Antolín, L. Beola, V. Grazú, R. M. Fratila, L. Gutiérrez and J. M. de la Fuente, *Adv. Drug Delivery Rev.*, 2019, **138**, 326–343.
19 J. F. Liu, B. Jang, D. Issadore and A. Tsourkas, *Wiley Interdiscip. Rev.: Nanomed. Nanobiotechnol.*, 2019, **11**, e1571.
20 S. Mura, J. Nicolas and P. Couvreur, *Nat. Mater.*, 2013, **12**, 991–1003.
21 J. Chen, Y. Zhu, C. Wu and J. Shi, *Chem. Soc. Rev.*, 2020, **49**, 9057–9094.
22 Y. Zhang, Y. Wang, Q. Zhou, X. Chen, W. Jiao, G. Li, M. Peng, X. Liu, Y. He and H. Fan, *ACS Appl. Mater. Interfaces*, 2021, **13**, 52395–52405.
23 R. Jauregui, S. Srinivasan, L. N. Vojtech, H. S. Gammill, D. T. Chiu, F. Hladik, P. S. Stayton and J. J. Lai, *ACS Appl. Mater. Interfaces*, 2018, **10**, 33847–33856.
24 D. Parasuraman, A. K. Sarker and M. J. Serpe, *ChemPhysChem*, 2012, **13**, 2507–2515.
25 Q. M. Kainz and O. Reiser, *Acc. Chem. Res.*, 2014, **47**, 667–677.
26 G. Hemery, E. Garanger, S. Lecommandoux, A. D. Wong, E. R. Gillies, B. Pedrono, T. Bayle, D. Jacob and O. Sandre, *J. Phys. D: Appl. Phys.*, 2015, **48**, 494001.
27 G. Huang, Y. Qiu, F. Yang, J. Xie, X. Chen, L. Wang and H. Yang, *Nano Lett.*, 2021, **21**, 2926–2931.
28 H. Huang, S. Delikanli, H. Zeng, D. M. Ferkey and A. Pralle, *Nat. Nanotechnol.*, 2010, **5**, 602–606.
29 J. G. Ovejero, I. Armenia, D. Serantes, S. Veintemillas-Verdaguer, N. Zeballos, F. López-Gallego, C. Grüttner, J. M. de la Fuente, M. d. Puerto Morales and V. Grazu, *Nano Lett.*, 2021, **21**, 7213–7220.
30 Z. J. Díaz-Puerto, Á. Raya-Barón, P. W. N. M. van Leeuwen, J. M. Asensio and B. Chaudret, *Nanoscale*, 2021, **13**, 12438–12442.
31 S. Faure, N. Mille, S. S. Kale, J. M. Asensio, J. Marbaix, P. Farger, D. Stoian, W. van Beek, P.-F. Fazzini, K. Soulantica, B. Chaudret and J. Carrey, *J. Phys. Chem. C*, 2020, **124**, 22259–22265.
32 H. C. Davis, S. Kang, J.-H. Lee, T.-H. Shin, H. Putterman, J. Cheon and M. G. Shapiro, *Biophys. J.*, 2020, **118**, 1502–1510.
33 J. T. Dias, M. Moros, P. del Pino, S. Rivera, V. Grazú and J. M. de la Fuente, *Angew. Chem., Int. Ed.*, 2013, **52**, 11526–11529.
34 G. Audran, E. G. Bagryanskaya, S. R. A. Marque and P. Postnikov, *Polymers*, 2020, **12**, 1481.
35 M. Edeleva, G. Audran, S. Marque and E. Bagryanskaya, *Materials*, 2019, **12**, 688.
36 E. G. Bagryanskaya and S. R. A. Marque, *Nitroxide Mediated Polymerization: From Fundamentals to Applications in Materials Science*, The Royal Society of Chemistry, 2016, pp. 45–113. DOI: 10.1039/9781782622635-00045.
37 D. Bertin, D. Gigmes, S. R. A. Marque and P. Tordo, *Chem. Soc. Rev.*, 2011, **40**, 2189–2198.
38 L. Larue, T. Moussounda Moussounda Koumba, N. Le Breton, B. Vileno, P. Arnoux, V. Jouan-Hureaux, C. Boura,

 This journal is © The Royal Society of Chemistry 2023

Open Access Article. Published on 20 October 2022. Downloaded on 8/2/2025 6:21:49 PM. This article is licensed under a Creative Commons Attribution-NonCommercial 3.0 Unported Licence.

G. Audran, R. Bikanga, S. R. A. Marque, S. Acherar and C. Frochot, *ACS Appl. Bio Mater.*, 2021, **4**, 1330–1339.

39 O. Guselnikova, G. Audran, J.-P. Joly, A. Trelin, E. V. Tretyakov, V. Svorcik, O. Lyutakov, S. R. A. Marque and P. Postnikov, *Chem. Sci.*, 2021, **12**, 4154–4161.

40 M. Albalat, G. Audran, M. Holzritter, S. R. A. Marque, P. Mellet, N. Vanthuyne and P. Voisin, *Org. Chem. Front.*, 2020, **7**, 2916–2924.

41 O. Guselnikova, S. R. A. Marque, E. V. Tretyakov, D. Mares, V. Jerabek, G. Audran, J.-P. Joly, M. Trusova, V. Svorcik, O. Lyutakov and P. Postnikov, *J. Mater. Chem. A*, 2019, **7**, 12414–12419.

42 G. Audran, L. Bosco, P. Brémond, N. Jugniot, S. R. A. Marque, P. Massot, P. Mellet, T. Moussounda Moussounda Koumba, E. Parzy, A. Rivot, E. Thiaudière, P. Voisin, C. Wedl and T. Yamasaki, *Org. Chem. Front.*, 2019, **6**, 3663–3672.

43 J. C. Scaiano, T. J. Connolly, N. Mohtat and C. N. Pliva, *Can. J. Chem.*, 1997, **75**, 92–97.

44 T. Reyser, T. H. To, C. Egwu, L. Paloque, M. Nguyen, A. Hamouy, J.-L. Stigliani, C. Bijani, J.-M. Augereau, J.-P. Joly, J. Portela, J. Havot, S. R. A. Marque, J. Boissier, A. Robert, F. Benoit-Vical and G. Audran, *Molecules*, 2020, **25**, 3838.

45 T. Yamasaki, D. Buric, C. Chacon, G. Audran, D. Braguer, S. R. A. Marque, M. Carré and P. Brémond, *Bioorg. Med. Chem.*, 2019, **27**, 1942–1951.

46 D. Moncelet, P. Voisin, N. Koonjoo, V. Bouchaud, P. Massot, E. Parzy, G. Audran, J.-M. Franconi, E. Thiaudière, S. R. A. Marque, P. Brémond and P. Mellet, *Mol. Pharm.*, 2014, **11**, 2412–2419.

47 W. W. Yu, J. C. Falkner, C. T. Yavuz and V. L. Colvin, *Chem. Commun.*, 2004, 2306–2307, DOI: 10.1039/B409601K.

48 L. Lartigue, C. Innocenti, J. Larionova and Y. Guari, *J. Nanosci. Nanotechnol.*, 2019, **19**, 5000–5007.

49 S. Kenouche, J. Larionova, N. Bezzi, Y. Guari, N. Bertin, M. Zanca, L. Lartigue, M. Cieslak, C. Godin, G. Morrot and C. Goze-Bac, *Powder Technol.*, 2014, **255**, 60–65.

50 L. Bordonali, T. Kalaivani, K. P. V. Sabareesh, C. Innocenti, E. Fantechi, C. Sangregorio, M. F. Casula, L. Lartigue, J. Larionova, Y. Guari, M. Corti, P. Arosio and A. Lascialfari, *J. Phys.: Condens. Matter*, 2013, **25**, 066008.

51 L. Lartigue, C. Innocenti, T. Kalaivani, A. Awwad, M. d. M. Sanchez Duque, Y. Guari, J. Larionova, C. Guérin, J.-L. G. Montero, V. Barragan-Montero, P. Arosio, A. Lascialfari, D. Gatteschi and C. Sangregorio, *J. Am. Chem. Soc.*, 2011, **133**, 10459–10472.

52 H. Benbenishty-Shamir, R. Gilert, I. Gotman, E. Y. Gutmanas and C. N. Sukenik, *Langmuir*, 2011, **27**, 12082–12089.

53 L. Lartigue, K. Oumzil, Y. Guari, J. Larionova, C. Guérin, J.-L. Montero, V. Barragan-Montero, C. Sangregorio, A. Caneschi, C. Innocenti, T. Kalaivani, P. Arosio and A. Lascialfari, *Org. Lett.*, 2009, **11**, 2992–2995.

54 O. U. Akakuru, M. Z. Iqbal, C. Liu, J. Xing, Z. Wei, Z. Jiang, Q. Fang, B. Yuan, E. I. Nosike, J. Xia, Y. Jin, J. Zheng and A. Wu, *Appl. Mater. Today*, 2020, **18**, 100524.

55 Y. Hou, Z. Xu and S. Sun, *Angew. Chem., Int. Ed.*, 2007, **46**, 6329–6332.

56 Y.-k. Sun, M. Ma, Y. Zhang and G. Ning, *Colloids Surf., A*, 2004, **245**, 15–19.

57 A. Okamura, S. Nakamura, M. Tanaka and K. Siratori, *J. Phys. Soc. Jpn.*, 1995, **64**, 3484–3495.

58 A. Mitra, J. Mohapatra, S. S. Meena, C. V. Tomy and M. Aslam, *J. Phys. Chem. C*, 2014, **118**, 19356–19362.

59 L. Néel, *Ann. Geophys.*, 1949, **5**, 99.

60 O. L. Lanier, O. I. Korotych, A. G. Monsalve, D. Wable, S. Savliwala, N. W. F. Grooms, C. Nacea, O. R. Tuitt and J. Dobson, *Int. J. Hyperthermia*, 2019, **36**, 686–700.

61 R. R. Wildeboer, P. Southern and Q. A. Pankhurst, *J. Phys. D: Appl. Phys.*, 2014, **47**, 495003.

62 S. Marque, C. Le Mercier, P. Tordo and H. Fischer, *Macromolecules*, 2000, **33**, 4403–4410.

63 L. Polo-Corrales and C. Rinaldi, *J. Appl. Phys.*, 2012, **111**, 07B334.